



Reduced net methane emissions due to microbial methane oxidation in a warmer Arctic

Youmi Oh¹, Qianlai Zhuang^{1,2,3}✉, Licheng Liu¹, Lisa R. Welp^{1,2}, Maggie C. Y. Lau^{4,9}, Tullis C. Onstott⁴, David Medvigy⁵, Lori Bruhwiler⁶, Edward J. Dlugokencky⁶, Gustaf Hugelius⁷, Ludovica D'Imperio⁸ and Bo Elberling⁸

Methane emissions from organic-rich soils in the Arctic have been extensively studied due to their potential to increase the atmospheric methane burden as permafrost thaws^{1–3}. However, this methane source might have been overestimated without considering high-affinity methanotrophs (HAMs; methane-oxidizing bacteria) recently identified in Arctic mineral soils^{4–7}. Herein we find that integrating the dynamics of HAMs and methanogens into a biogeochemistry model^{8–10} that includes permafrost soil organic carbon dynamics³ leads to the upland methane sink doubling ($-5.5 \text{ Tg CH}_4 \text{ yr}^{-1}$) north of 50°N in simulations from 2000–2016. The increase is equivalent to at least half of the difference in net methane emissions estimated between process-based models and observation-based inversions^{11,12}, and the revised estimates better match site-level and regional observations^{5,7,13–15}. The new model projects doubled wetland methane emissions between 2017–2100 due to more accessible permafrost carbon^{16–18}. However, most of the increase in wetland emissions is offset by a concordant increase in the upland sink, leading to only an 18% increase in net methane emission (from 29 to 35 $\text{Tg CH}_4 \text{ yr}^{-1}$). The projected net methane emissions may decrease further due to different physiological responses between HAMs and methanogens in response to increasing temperature^{19,20}.

Arctic soils are considered to be a substantial net emission source of methane to the atmosphere. Current process-based biogeochemistry models and observation-based atmospheric inversions have estimated this source to be between 15 and 50 $\text{Tg CH}_4 \text{ yr}^{-1}$, which accounts for 20–25% of global natural methane emissions¹². Furthermore, process-based models predict that methane emissions will be two to three times greater by 2100^{2,17,18}, as warmer temperatures will increase both the rate of decomposition and availability of soil organic carbon (SOC) from permafrost-affected soils in addition to SOC from recently dead vegetation for decomposition^{16,21}.

However, methane emissions are mainly confined to the 13% of Arctic landscapes composed of organic-rich soils where anaerobic processes dominate¹⁶. The rest are composed of mineral-rich soils, from which recent field studies have identified net annual methane sinks during growing seasons^{1–7}. This difference may be controlled by differences in methanotroph community composition (Fig. 1)²². In wet organic soils, a fraction of methane produced by methanogenic archaea (methanogens, MGs) is oxidized by methanotrophic

bacteria (methanotrophs) and the remainder is mostly emitted into the atmosphere (Fig. 1a). The methanotrophs in these wet organic soils may be low-affinity methanotrophs (LAMs) that require >600 ppm of methane (by moles) for their growth and maintenance²³. But in dry mineral soils, the dominant methanotrophs are high-affinity methanotrophs (HAMs), which can survive and grow at a level of atmospheric methane abundance ($[\text{CH}_4]_{\text{atm}}$) of about 1.8 ppm (Fig. 1b)²⁴.

Quantification of the previously underestimated HAM-driven methane sink is needed to improve our understanding of Arctic methane budgets. Process-based methane models have overestimated Arctic methane emission by 5–10 $\text{Tg CH}_4 \text{ yr}^{-1}$ when compared with observation-based atmospheric inversions^{11,12}. Given that 87% of the Arctic is dominated by mineral-rich soils, the HAM-driven methane sink may greatly reduce current area-integrated net methane emissions. Furthermore, the positive feedbacks of methane emission that result from additional accessible permafrost soil organic carbon (PSOC) may be partially suppressed by negative feedbacks from the high activities of HAMs at future increased surface temperatures and $[\text{CH}_4]_{\text{atm}}$ (ref. 8).

Previous studies show that simulation of explicit microbial dynamics of MGs and HAMs improve model estimates of the magnitude and seasonality of methane sources and sinks^{8,25}. Microbial dynamics may also cause additional complexity due to different microbial physiology between MGs and HAMs^{19,26}. Recent laboratory and field studies show that microbial communities adjust their active microbial biomass ($\text{MIC}_{\text{biomass}}$) in warmer soils depending on the microbial growth efficiency (ϵ) and maintenance energy (m_E)¹⁹; ϵ represents the growth efficiency of $\text{MIC}_{\text{biomass}}$ per unit of substrate consumed and it is a factor of ten smaller for MGs ($\epsilon=0.05$) than for HAMs ($\epsilon=0.5$)^{20,27}; m_E (that is, the rate of metabolic energy generation needed to maintain $\text{MIC}_{\text{biomass}}$) increases exponentially with temperature for all microbes, including MGs and HAMs, reflecting the fast turnover associated with cell mortality (equation (16))^{19,28}. These processes are important for current and future Arctic methane budgets; however, current process-based methane models have not considered such microbial dynamics.

First, this study estimates current pan-Arctic soil methane emissions and consumptions while accounting for microbial and PSOC dynamics; second, it evaluates the magnitude and spatial variability of those estimates; and, third, projects pan-Arctic changes in

¹Department of Earth, Atmospheric, and Planetary Sciences, Purdue University, West Lafayette, IN, USA. ²Purdue Climate Change Research Center, West Lafayette, IN, USA. ³Department of Agronomy, Purdue University, West Lafayette, IN, USA. ⁴Department of Geosciences, Princeton University, Princeton, NJ, USA. ⁵Department of Biological Sciences, University of Notre Dame, Notre Dame, IN, USA. ⁶NOAA Earth System Research Laboratory, Global Monitoring Division, Boulder, CO, USA. ⁷Department of Physical Geography and Bolin Centre for Climate Research, Stockholm University, Stockholm, Sweden. ⁸Center for Permafrost (CENPERM), University of Copenhagen, Copenhagen, Denmark. ⁹Present address: Laboratory of Extraterrestrial Ocean Systems, Institute of Deep-sea Science and Engineering, Chinese Academy of Sciences, Sanya, China. ✉e-mail: qzhuang@purdue.edu

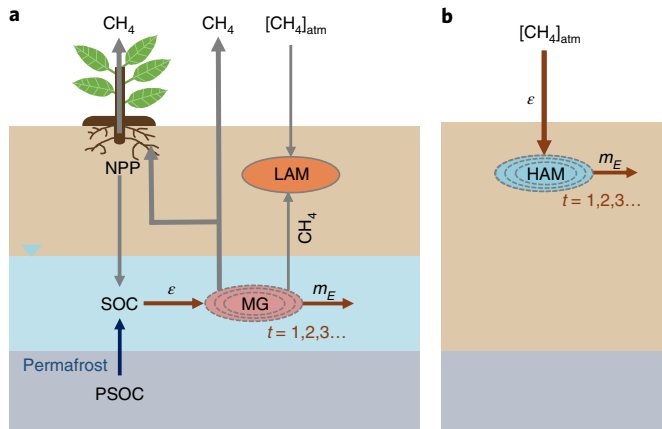


Fig. 1 | A schematic diagram of XPTEM-XHAM. a, b. The model simulates CH_4 production by MGs and oxidation of CH_4 by LAMs in wetlands (a) as well as the oxidation of $[\text{CH}_4]_{\text{atm}}$ by HAMs in uplands (b). We used static inundation data³³ to divide the Arctic landscape into wetland and upland regions but later varied the regions on the basis of time-varying inundation data^{34,35}. Changes in $\text{MIC}_{\text{biomass}}$ of MGs and HAMs (grey dashed lines) depend on ε and m_E , and are tracked as a function of time (t (h)). PSOC dynamics are added to account for SOC that is accessible from thawing permafrost when soil temperatures at the corresponding depths become higher than 1°C . The dark blue arrow refers to PSOC dynamics, dark red arrows refer to microbial dynamics and grey arrows refer to processes from the original TEM.

soil methane emissions and consumptions through 2100. These projections take into account enhanced methane emissions due to increased available PSOC and stimulated HAM methane consumptions, as well as the different physiological responses of MGs and HAMs at warmer temperatures.

To address these objectives, we implemented explicit microbial dynamics for MGs and HAMs into a biogeochemistry model; that is, the terrestrial ecosystem model (TEM) (Fig. 1)^{9,10}. In a wetland system, we simulated methane oxidation by LAMs as a function of environmental parameters. We fixed LAM $\text{MIC}_{\text{biomass}}$ due to its limited control on Arctic wetland methane emissions (Supplementary Method 6)^{29,30}. We thus calculated changes in $\text{MIC}_{\text{biomass}}$ of MGs and HAMs as a function of ε , m_E and environmental parameters, and set m_E as a constant with a temperature of 0°C (refs. 19,28). To identify the effects of PSOC, we modified methane production to consider the amount of SOC from vegetation (net primary productivity, NPP) and thawing permafrost in wetland ecosystems. The complete model with microbial and PSOC dynamics is referred to as the explicit permafrost TEM-explicit HAM model (XPTEM-XHAM, Fig. 1; see Methods).

We conducted two additional sets of simulations for a factorial analysis to assess the effects of microbial and PSOC dynamics (Table 1). First, we developed the permafrost TEM-HAM model (PTEM-HAM), which considers HAMs and PSOC as XPTEM-XHAM does, but does not simulate the explicit microbial dynamics of MGs and HAMs. Second, we used a version of TEM that simulates the production and oxidation of methane by MGs and LAMs, respectively, but that does not consider HAMs, permafrost nor microbial dynamics (denoted TEM)^{9,10}. For XPTEM-XHAM and PTEM-HAM, we optimized key parameters of methane production and oxidation for alpine tundra, wet tundra and boreal forest (see Methods and Supplementary Methods).

The three models simulated methane dynamics north of 50°N , including low- ($50\text{--}65^\circ\text{N}$) and high- (north of 65°N) Arctic regions at a spatial resolution of 0.5° latitude by 0.5° longitude. Gridded

Table 1 | A summary of the three models used in this study

Model set-up	XPTEM-XHAM	PTEM-HAM	TEM
PSOC dynamics	On	On	Off
HAMs	On	On	Off
Microbial dynamics of HAMs and MGs	On	Off	Off

The set-up for XPTEM-XHAM is explained in detail in Fig. 1. For PTEM-HAM, the production of methane in wetlands is dependent on SOC derived from vegetation and thawing permafrost; methane is oxidized by HAMs, but $\text{MIC}_{\text{biomass}}$ changes are not explicitly simulated. In the set-up of TEM, the production of methane in wetlands is dependent on SOC derived from vegetation only, methane is oxidized by LAMs only, and $\text{MIC}_{\text{biomass}}$ changes are also not explicitly simulated.

Climatic Research Unit (CRU) data were used as meteorological inputs for a contemporary simulation from 2000 to 2016³¹, and inputs from IPCC representative concentration pathways (RCPs) 2.6, 4.5 and 8.5 were used for projections to 2100³². For PTEM-HAM and XPTEM-XHAM, we used the Northern Circumpolar Soil Carbon Database v.2 (NCSCDv2) to estimate PSOC at different soil depths¹⁶. The simulated methane emission from wetlands and consumption from uplands were area-integrated for each grid cell on the basis of static fractional inundation data³³.

For a sensitivity test of the surface area of the wetlands and uplands of XPTEM-XHAM, we used time-varying inundation data from the Satellite-driven Surface Water Microwave Product Series—Global Lakes and Wetlands Database (SWAMPS-GLWD) from 2000 to 2012³⁴ and transient inundation fraction simulated by Community Land Model v.5.0 from 2017 to 2100³⁵. We further conducted XPTEM-XHAM sensitivity tests of wetland emission and upland consumption to changes in meteorology and substrate inputs from 2000 to 2016. For XPTEM-XHAM from 2017–2100, we varied m_E of MGs and HAMs to increase with temperature to model microbial physiological responses (equations (13C), (13D) and (16)). Finally, for RCP 8.5 of XPTEM-XHAM, we varied coenzyme Q_{10} for methane production and oxidation, and fixed $[\text{CH}_4]_{\text{atm}}$ to the contemporary level (1.8 ppm) to test model sensitivity to temperature and $[\text{CH}_4]_{\text{atm}}$ changes (see Methods and Supplementary Methods).

Our simulations from 2000 to 2016 show the effects of PSOC and microbial dynamics on wetland methane emissions (Fig. 2a, Extended Data Figs. 1–3, Supplementary Figs. 7 and 8, Supplementary Table 8). Compared with PTEM-HAM, TEM estimates larger wetland methane emissions in the low-Arctic (37.70 versus $26.83 \text{ Tg CH}_4 \text{ yr}^{-1}$) but smaller emissions in the high-Arctic (3.73 versus $6.76 \text{ Tg CH}_4 \text{ yr}^{-1}$). TEM simulates higher emissions in the low-Arctic as its parameterization on substrate depends only on NPP, which is higher in the low-Arctic (Extended Data Fig. 3c). For PTEM-HAM, methane emission is based on NPP and PSOC, with more prevalent PSOC in the high-Arctic (Extended Data Fig. 3d). In comparison with PTEM-HAM, XPTEM-XHAM simulates larger methane wetland emissions in the low-Arctic ($32.60 \text{ Tg CH}_4 \text{ yr}^{-1}$) due to the high $\text{MIC}_{\text{biomass}}$ of MGs that persists late into the growing season, extending the period of methane emissions (Extended Data Fig. 1)²⁵.

By comparing the results from XPTEM-XHAM and TEM, we more than double the upland methane sink by including microbially dynamic HAMs (Fig. 2b). TEM estimates upland sinks of $4.16 \text{ Tg CH}_4 \text{ yr}^{-1}$ north of 50°N . After considering HAM and microbial dynamics, upland sinks for PTEM-HAM and XPTEM-XHAM increase to 6.15 and $9.52 \text{ Tg CH}_4 \text{ yr}^{-1}$, respectively, which is consistent for both the low- and high-Arctic. This additional $\sim 5.5 \text{ Tg CH}_4 \text{ yr}^{-1}$ has not been accounted for in most current process-based methane models that do not consider microbial dynamics of HAMs^{1,17,18}.

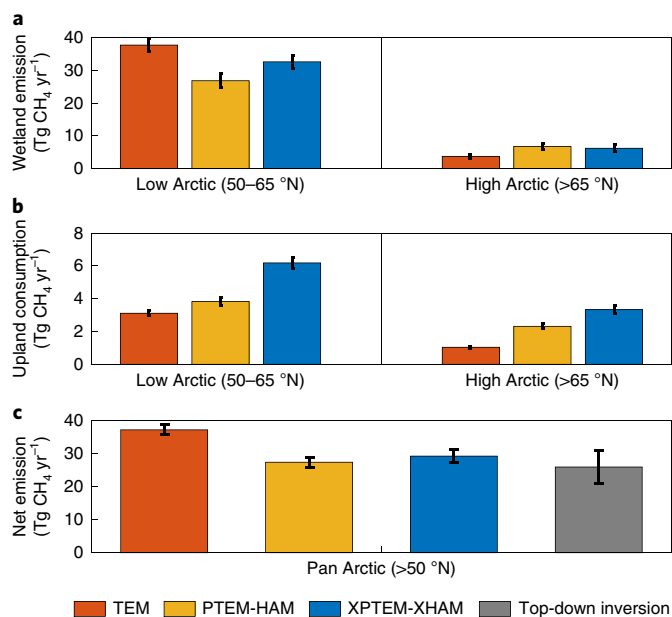


Fig. 2 | Annual estimates of the Arctic methane budget by three models for 2000–2016. a–c, Annual estimates of wetland methane emission (**a**), upland methane consumption (**b**) and net methane emission (**c**) averaged over 2000–2016 for TEM (red), PTEM-HAM (yellow) and XPTM-XHAM (blue) for the pan-Arctic region (north of 50°N), including the low-Arctic between 50–65°N and high-Arctic north of 65°N. The error bars represent 1σ of TEM, PTEM-HAM and XPTM-XHAM, which were determined by varying the optimized parameters from ensemble simulations. The top-down inversion in **c** (grey) represents posterior estimates of mean and 1σ of net wetland methane fluxes by CarbonTracker-CH₄ in 2000–2010 (ref. 11).

By integrating wetland emission and upland consumption, net Arctic methane emission of XPTM-XHAM and PTEM-HAM are closer to posterior fluxes estimated by an observation-based inversion, CarbonTracker-CH₄ (Fig. 2c)¹¹. Starting with a previous estimate of $35 \pm 10 \text{ Tg CH}_4 \text{ yr}^{-1}$ for wetland emissions north of 50°N, CarbonTracker-CH₄ reduced net emission to $26 \pm 5 \text{ Tg CH}_4 \text{ yr}^{-1}$ during its optimization. Our estimates of increased upland methane

sinks are equivalent to at least half of the difference between estimates from before and after the inversion^{11,12}.

From 2000 to 2012, our XPTM-XHAM sensitivity test using time-varying inundation data simulates less Arctic net methane emission due to smaller annual inundation fraction in SWAMPS-GLWD compared with the static map north of 50°N (Extended Data Fig. 4 and Supplementary Fig. 9)^{33,34}. Additional sensitivity tests to meteorological and substrate changes show that wetland emission is sensitive to temperature, NPP, PSOC and water table depth, whereas upland consumption is sensitive to temperature, soil moisture and $[\text{CH}_4]_{\text{atm}}$ (Supplementary Fig. 10).

We validated the magnitude and spatial variability of the three models using site-level and regional observations (see Methods). In situ measurements from 46 flux observation sites confirm that XPTM-XHAM reproduces both methane emission and consumption (with R^2 values of 0.65 and 0.87, and r.m.s.e. values of 38.21 and 0.52 $\text{mg m}^{-2} \text{ d}^{-1}$, respectively) (Supplementary Table 5 and Extended Data Fig. 5)⁵⁷. Compared with XPTM-XHAM, r.m.s.e. values in PTEM-HAM and TEM were 10% and 60% larger, respectively, on average for all sites. We also compared the observed and simulated regional net methane fluxes of three regions for emission (Alaska, Hudson Bay Lowlands, West Siberian Lowlands) and two for consumption (Northeast and West Greenland) (Fig. 3a, Supplementary Fig. 8, and Supplementary Tables 6 and 7)^{4,6,13–15}. XPTM-XHAM generally matched emission estimates for the West Siberian Lowlands and consumption in upland West Greenland, whereas PTEM-XHAM and TEM agreed poorly. All three models estimate less methane emissions from Alaska than observed¹⁵, possibly because we did not consider methane emissions from aquatic sources such as thermokarst lakes³⁶.

Our future simulation shows that both PTEM-HAM and XPTM-XHAM project 70 and 100% increase in wetland methane emissions by 2100 for RCP 8.5, respectively, due to increased temperature and more accessible PSOC (Figs. 3b, 4a and Supplementary Fig. 11). This increase is larger than the 59% increase predicted by TEM. However, the increase in wetland emission is mostly compensated by an increase in upland consumption by 2100 (22 and 35 $\text{Tg CH}_4 \text{ yr}^{-1}$ for PTEM-HAM and XPTM-XHAM, respectively) due to increased HAM activity at increased temperature and $[\text{CH}_4]_{\text{atm}}$ (Supplementary Figs. 11–13). This leads to a reduced increase in net methane emission by 2100 for XPTM-XHAM and PTEM-HAM (35 $\text{Tg CH}_4 \text{ yr}^{-1}$) when compared with TEM (55 $\text{Tg CH}_4 \text{ yr}^{-1}$) and

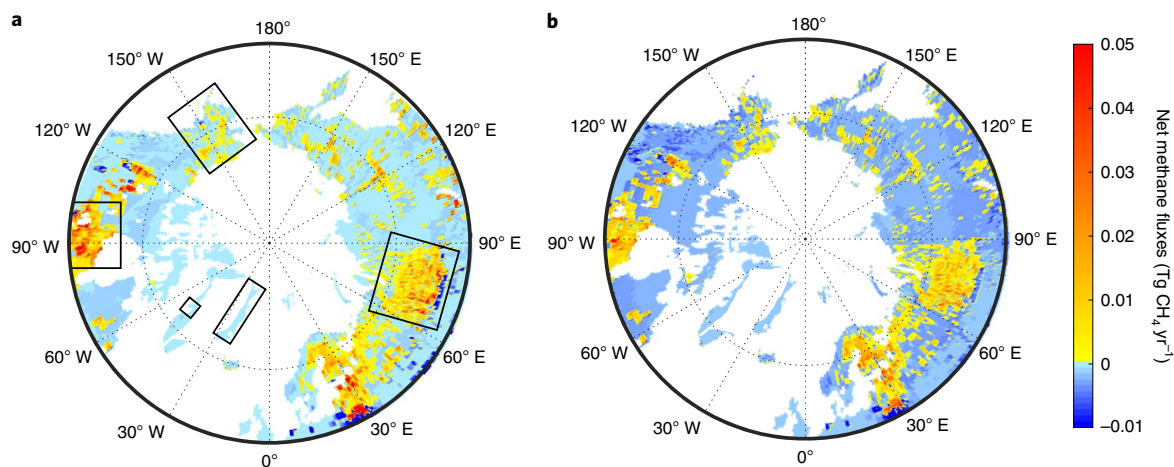


Fig. 3 | The spatial variability of annual net methane flux north of 50°N for XPTM-XHAM. a, b, The net methane fluxes (positive for emission and negative for consumption) averaged for the contemporary period during 2000–2016 (**a**), as well as the difference between 2086–2100 and 2000–2016 for RCP 8.5 (**b**), are shown. The dotted longitudes are at 30° intervals and the dotted latitude is at 65°N. Panel **a** also shows the five regions used for regional model-data comparisons (black boxes) (Supplementary Tables 6 and 7).

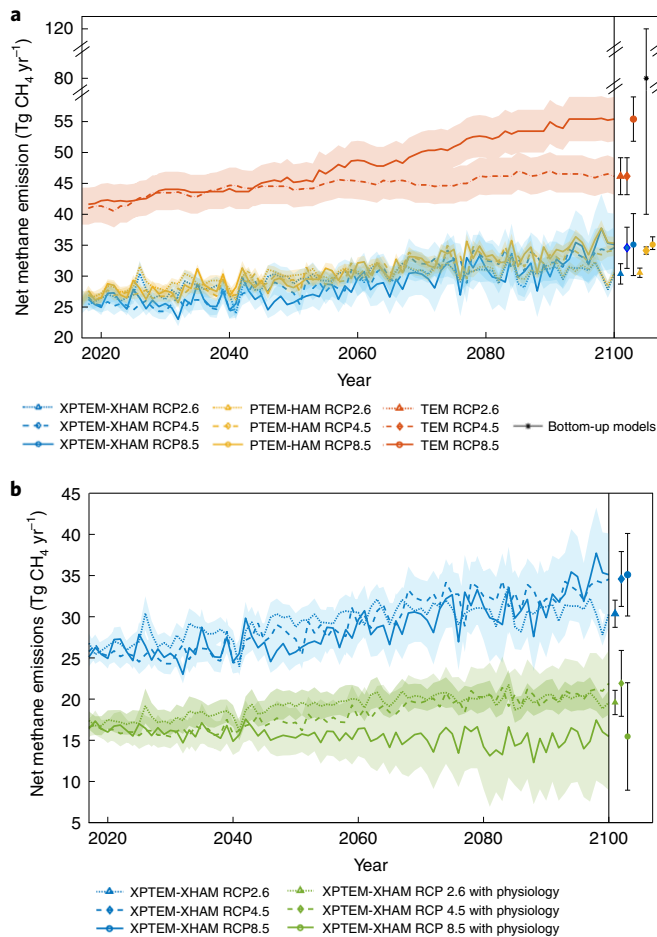


Fig. 4 | Projected annual net Arctic methane emissions from 2017 to 2100 north of 50°N. a, Annual estimates of pan-Arctic net methane emission for XPTEM-XHAM (baseline, blue), PTEM-HAM (yellow) and TEM (red). **b**, Annual estimates of pan-Arctic net methane emission for XPTEM-XHAM (blue) and XPTEM-XHAM with physiological responses of MG and HAM to temperature change with varying m_E (green), based on RCPs 2.6 (dotted), 4.5 (dashed) and 8.5 (solid). The shaded error bars represent 1σ of TEM, PTEM-HAM and XPTEM-XHAM, and were determined by varying the optimized parameters from ensemble simulations. The mean (symbols) and 1σ (bars) in 2100 for each metric are shown to the right in both **a** and **b**. Panel **a** also shows mean (*) and 1σ (bars) of previous estimates of net methane emission estimated by process-based methane models^{2,17,18}.

other previous projections (40–120 Tg CH₄ yr⁻¹)^{2,17,18}. The net methane emission increase is less for RCP 2.6 and 4.5 than for RCP 8.5 in all three models (Fig. 4a and Supplementary Fig. 11).

Furthermore, our simulation of XPTEM-XHAM, which incorporates microbial physiology of MGs and HAMs with varying m_E , shows that net Arctic methane emission can potentially decrease in the future (Fig. 4b and Supplementary Fig. 14). Increases in both methane production and oxidation are limited by decreases in MIC_{biomass} growth for MGs and HAMs, respectively, due to an exponential increase in m_E (equation (16))^{19,28}. As m_E increases with temperature, growth in MIC_{biomass} slows more substantially for MG, because the ϵ of MGs (0.05) is a factor of ten smaller than the ϵ of HAMs (0.5)^{20,27}. As a result, in our simulation, HAMs survive better in the warmer Arctic due to their physiological response.

Our sensitivity test of XPTEM-XHAM using time-varying inundation simulated by community land model 5.0 does not change the projection considerably as the simulated inundation fraction increases by only 5% between 2017 and 2100

(Extended Data Fig. 6)³⁵. XPTEM-XHAM also shows a sensitivity of net methane emissions to both temperature (5 Tg CH₄ yr⁻¹) and [CH₄]_{atm} (10 Tg CH₄ yr⁻¹) by 2100 for the RCP 8.5 scenario (Supplementary Fig. 15).

Our simulation emphasizes that the current understanding of Arctic methane feedback may be incomplete (Extended Data Fig. 7)⁸. Previous studies predicted strong positive feedbacks between temperature and methane emission due to more accessible SOC from thawing permafrost; however, additional negative feedbacks between temperature and HAMs may suppress this feedback loop. This study also shows we need more field and laboratory experiments to understand HAM and MG physiological responses to environmental changes^{22,37}.

Although the new model significantly revises estimates of net Arctic methane emission, there are processes that current models, including ours, have not considered. We do not capture the complex Arctic hydrological and vegetation dynamics^{38,39}, which may influence our estimates of both methane production and consumption. We focused on terrestrial ecosystems without considering potential large methane emissions from aquatic systems, whose magnitude and spatial distribution may change^{36,40}. We used observed wetland methane emissions to optimize methane production and oxidation where the fraction of each is uncertain²⁵. More observations of subsurface vertical processes using isotopic labelling analysis and inhibitor techniques will better constrain future models⁴¹.

In conclusion, we show that the microbial dynamics of HAMs are an important component of the current Arctic methane budget as our estimate more than doubles that of upland sinks. We also find that our revised estimates, which incorporate microbial and PSOC dynamics, better match site-level and regional observations and observation-based inversions. This model projects a smaller increase in net methane emission by 2100 than previous models, as the increase in wetland emission (due to more accessible PSOC) is mostly offset by the increase in upland consumption by HAMs. A potential decrease in future net methane emission is projected after including the microbial physiology of HAMs and MGs. This study highlights the need to incorporate more detailed microbial dynamics into process-based methane models to better constrain the Arctic methane budget.

Online content

Any methods, additional references, Nature Research reporting summaries, source data, extended data, supplementary information, acknowledgements, peer review information; details of author contributions and competing interests; and statements of data and code availability are available at <https://doi.org/10.1038/s41558-020-0734-z>.

Received: 8 October 2019; Accepted: 13 February 2020;

Published online: 30 March 2020

References

- McGuire, A. D. et al. Dependence of the evolution of carbon dynamics in the northern permafrost region on the trajectory of climate change. *Proc. Natl Acad. Sci. USA* **115**, 3882–3887 (2018).
- Schuur, E. A. G. et al. Expert assessment of vulnerability of permafrost carbon to climate change. *Clim. Change* **119**, 359–374 (2013).
- Schuur, E. A. G. et al. Climate change and the permafrost carbon feedback. *Nature* **520**, 171–179 (2015).
- Juncher Jørgensen, C., Lund Johansen, K. M., Westergaard-Nielsen, A. & Elberling, B. Net regional methane sink in High Arctic soils of northeast Greenland. *Nat. Geosci.* **8**, 20–23 (2015).
- Lau, M. C. Y. et al. An active atmospheric methane sink in high Arctic mineral cryosols. *ISME J.* **9**, 1880–1891 (2015).
- D’Imperio, L., Nielsen, C. S., Westergaard-Nielsen, A., Michelsen, A. & Elberling, B. Methane oxidation in contrasting soil types: responses to experimental warming with implication for landscape-integrated CH₄ budget. *Glob. Chang. Biol.* **23**, 966–976 (2017).

7. Emmerton, C. A. et al. The net exchange of methane with high Arctic landscapes during the summer growing season. *Biogeosciences* **11**, 3095–3106 (2014).
8. Oh, Y. et al. A scalable model for methane consumption in arctic mineral soils. *Geophys. Res. Lett.* **43**, 5143–5150 (2016).
9. Zhuang, Q. et al. Methane fluxes between terrestrial ecosystems and the atmosphere at northern high latitudes during the past century: A retrospective analysis with a process-based biogeochemistry model. *Global Biogeochem. Cy.* **18**, GB3010 (2004).
10. Zhuang, Q. et al. Response of global soil consumption of atmospheric methane to changes in atmospheric climate and nitrogen deposition. *Global Biogeochem. Cy.* **27**, 650–663 (2013).
11. Bruhwiler, L. et al. CarbonTracker-CH₄: an assimilation system for estimating emissions of atmospheric methane. *Atmos. Chem. Phys.* **14**, 8269–8293 (2014).
12. Saunio, M. et al. The global methane budget 2000–2012. *Earth Syst. Sci. Data* **8**, 697–751 (2016).
13. Bloom, A. A., Palmer, P. I., Fraser, A., Reay, D. S. & Frankenberg, C. Large-scale controls of methanogenesis inferred from methane and gravity spaceborne data. *Science* **327**, 322–325 (2010).
14. Bohn, T. J. et al. WETCHIMP-WSL: intercomparison of wetland methane emissions models over West Siberia. *Biogeosciences* **12**, 3321–3349 (2015).
15. Miller, S. M. et al. A multiyear estimate of methane fluxes in Alaska from CARVE atmospheric observations. *Global Biogeochem. Cy.* **30**, 1441–1453 (2016).
16. Hugelius, G. et al. A new data set for estimating organic carbon storage to 3 m depth in soils of the northern circumpolar permafrost region. *Earth Syst. Sci. Data* **5**, 393–402 (2013).
17. Koven, C. D. et al. Permafrost carbon-climate feedbacks accelerate global warming. *Proc. Natl Acad. Sci. USA* **108**, 14769–14774 (2011).
18. Lawrence, D. M., Koven, C. D., Swenson, S. C., Riley, W. J. & Slater, A. G. Permafrost thaw and resulting soil moisture changes regulate projected high-latitude CO₂ and CH₄ emissions. *Environ. Res. Lett.* **10**, 094011 (2015).
19. Hagerty, S. B. et al. Accelerated microbial turnover but constant growth efficiency with warming in soil. *Nat. Clim. Change* **4**, 903–906 (2014).
20. Trimmer, M. et al. Riverbed methanotrophy sustained by high carbon conversion efficiency. *ISME J.* **9**, 2304–2314 (2015).
21. Schuur, E. A. G. et al. The effect of permafrost thaw on old carbon release and net carbon exchange from tundra. *Nature* **459**, 556–559 (2009).
22. Christiansen, J. R. et al. Methane fluxes and the functional groups of methanotrophs and methanogens in a young Arctic landscape on Disko Island, West Greenland. *Biogeochemistry* **122**, 15–33 (2015).
23. Baani, M. & Liesack, W. Two isozymes of particulate methane monooxygenase with different methane oxidation kinetics are found in *Methylocystis* sp. strain SC2. *Proc. Natl Acad. Sci. USA* **105**, 10203–10208 (2008).
24. Tveit, A. T. et al. Widespread soil bacterium that oxidizes atmospheric methane. *Proc. Natl Acad. Sci. USA* **116**, 8515–8524 (2019).
25. Segers, R. Methane production and methane consumption: a review of processes underlying wetland methane fluxes. *Biogeochemistry* **41**, 23–51 (1998).
26. Wieder, W. R., Bonan, G. B. & Allison, S. D. Global soil carbon projections are improved by modelling microbial processes. *Nat. Clim. Change* **3**, 909–912 (2013).
27. Von Stockar, U. & Liu, J. S. Does microbial life always feed on negative entropy? Thermodynamic analysis of microbial growth. *Biochim. Biophys. Acta Bioenerg.* **1412**, 191–211 (1999).
28. Tjhuis, L., Van Loosdrecht, M. C. M. & Heijnen, J. J. A thermodynamically based correlation for maintenance gibbs energy requirements in aerobic and anaerobic chemotrophic growth. *Biotechnol. Bioeng.* **42**, 509–519 (1993).
29. Knoblauch, C., Spott, O., Evgrafova, S., Kutzbach, L. & Pfeiffer, E. Regulation of methane production, oxidation, and emission by vascular plants and bryophytes in ponds of the northeast Siberian polygonal tundra. *J. Geophys. Res. Biogeosci.* **120**, 2525–2541 (2015).
30. Throckmorton, H. M. et al. Active layer hydrology in an arctic tundra ecosystem: quantifying water sources and cycling using water stable isotopes. *Hydrol. Process.* **30**, 4972–4986 (2016).
31. Harris, I., Jones, P. D., Osborn, T. J. & Lister, D. H. Updated high-resolution grids of monthly climatic observations—the CRU TS3.10 Dataset. *Int. J. Climatol.* **34**, 623–642 (2014).
32. Meinshausen, M. et al. The RCP greenhouse gas concentrations and their extensions from 1765 to 2300. *Clim. Change* **109**, 213–241 (2011).
33. Matthews, Elaine & Fung, I. Methane emission from natural wetlands: global distribution, area, and environmental characteristics of sources. *Global Biogeochem. Cy.* **1**, 61–86 (1987).
34. Poulter, B. et al. Global wetland contribution to 2000–2012 atmospheric methane growth rate dynamics. *Environ. Res. Lett.* **12**, 094013 (2017).
35. Lawrence, D. et al. *Technical Description of Version 5.0 of the Community Land Model (CLM) 4245–4287* (The National Center for Atmospheric Research, 2018).
36. Sepulveda-Jauregui, A., Walter Anthony, K. M., Martinez-Cruz, K., Greene, S. & Thalasso, F. Methane and carbon dioxide emissions from 40 lakes along a north-south latitudinal transect in Alaska. *Biogeosciences* **12**, 3197–3223 (2015).
37. McCalley, C. K. et al. Methane dynamics regulated by microbial community response to permafrost thaw. *Nature* **514**, 478–481 (2014).
38. Liljedahl, A. K. et al. Pan-Arctic ice-wedge degradation in warming permafrost and its influence on tundra hydrology. *Nat. Geosci.* **9**, 312–318 (2016).
39. Nauta, A. L. et al. Permafrost collapse after shrub removal shifts tundra ecosystem to a methane source. *Nat. Clim. Change* **5**, 67–70 (2015).
40. Wik, M., Varner, R. K., Anthony, K. W., MacIntyre, S. & Bastviken, D. Climate-sensitive northern lakes and ponds are critical components of methane release. *Nat. Geosci.* **9**, 99–105 (2016).
41. Pedersen, E. P., Michelsen, A. & Elberling, B. In situ CH₄ oxidation inhibition and ¹³CH₄ labeling reveal methane oxidation and emission patterns in a subarctic heath ecosystem. *Biogeochemistry* **138**, 197–213 (2018).

Publisher's note Springer Nature remains neutral with regard to jurisdictional claims in published maps and institutional affiliations.

© The Author(s), under exclusive licence to Springer Nature Limited 2020

Methods

Model description. We incorporated explicit microbial dynamics of HAMs and MGs—including PSOC dynamics—into TEM, a process-based biogeochemistry model.

TEM. TEM is one of few biogeochemistry models that simulate net methane consumption in Arctic mineral soils, and its methane, soil thermal and hydrological dynamics have been evaluated in previous studies^{9,10}. The methane dynamics module of TEM simulates methane production, oxidation and three transport processes between soil and atmosphere. In a wetland system, changes in methane concentrations (C_{Me}) at depth z and time t ($\partial C_{Me}(z,t)/\partial t$) are governed by equation (1), where $M_{prod}(z,t)$, $M_{oxid}(z,t)$, $R_{pl}(z,t)$ and $R_c(z,t)$ are methane production, oxidation, plant-mediated transport and ebullition rates, respectively, and $\partial F_{div}(z,t)/\partial z$ represents flux divergence due to gaseous and aqueous diffusion.

$$\frac{\partial C_{Me}(z,t)}{\partial t} = M_{prod}(z,t) - M_{oxid}(z,t) - \frac{\partial F_{div}(z,t)}{\partial z} - R_{pl}(z,t) - R_c(z,t) \dots \quad (1)$$

Methane is produced in anaerobic soils by MGs and is calculated by the product of maximum potential production rate (M_{GO}) and limiting functions of organic matter (OM) substrate, soil temperature, pH and redox potentials (S_{OM} , T_{soil} , H and X , respectively) (equation (2)). We used limiting factors of H and X to consider enzymatic activity and the relative availability of electron acceptors (for example, O_2 , NO_3^- , SO_4^{2-} , Fe^{+3} , Mn^{+2}) for methane production. The limiting function of substrate ($f(S_{OM}(z,t))$) is mainly dependent on SOC derived from vegetation (NPP), where NPP_{mon} is monthly NPP ($gC\ m^{-2}\ month^{-1}$), NPP_{max} is ecosystem-specific maximum monthly NPP and $f(C_{DIS}(z))$ describes the relative distribution of organic matter substrate at depth z (equation (3)). For the substrate availability, we calculated changes in vegetation carbon using atmospheric CO_2 concentrations, transient temperature, precipitation, vapour pressure and soil texture⁴².

$$M_{prod,TEM}(z,t) = M_{GO}f(S_{OM}(z,t))f(T_{soil}(z,t))f(H(z,t))f(X(z,t)) \dots \quad (2)$$

$$f(S_{OM}(z,t)) = \left(1 + \frac{NPP_{mon}}{NPP_{max}}\right)f(C_{DIS}(z)) \dots \quad (3)$$

The produced methane diffuses into aerobic soils and is oxidized by LAMs, which is calculated as the product of the maximum potential oxidation rate (O_{max}) and limiting functions of methane concentration, soil temperature, soil moisture, redox potential, nitrogen deposition, diffusion limited by high soil moisture and oxygen concentration (C_{Me} , T_{soil} , E_{SM} , R_{ox} , N_{dp} , D_{SM} and CO_2 , respectively) (equation (4)). The Michaelis–Menten constant for methane oxidation was set to $5\ \mu M$ ($k_{Me,LAM}$) (equation (5))^{9,23}.

$$M_{oxid,TEM}(z,t) = O_{max}f(C_{Me}(z,t))f(T_{soil}(z,t))f(E_{SM}(z,t))f(R_{ox}(z,t))f(N_{dp}(z,t))f(D_{SM}(z,t))f(CO_2(z)) \dots \quad (4)$$

$$f(C_{Me}(z,t)) = \frac{C_{Me}(z,t)}{k_{Me,LAM} + C_{Me}(z,t)} \dots \quad (5)$$

The residual methane is emitted to the surface through three transport processes. First, gaseous and aqueous diffusion occur due to concentration gradients of methane ($\partial C_{Me}(z,t)/\partial t$) following Fick's law through soil pores (equation (6)). The molecular diffusion coefficient (D) in different soil layers was calculated based on soil texture and soil moisture. We also have a simple limitation of diffusion on temperature, that there will be no diffusion when temperature is below $0^\circ C$. Second, ebullition occurs when methane bubble forms (that is, when C_{Me} is greater than $500\ \mu mol\ l^{-1}$ in saturated soils) $f_{e(C_{Me}(z,t))}$; $f_{e(C_{Me}(z,t))}$ is multiplied by a constant rate of $1.0\ h^{-1}$ (K_e) (equation (7)).

Finally, plant-mediated transport occurs through the root systems of some plants that provide a direct conduit for methane to the atmosphere, and is a function of the rate constant of $0.01\ h^{-1}$, vegetation type, root density, vegetation growth and soil methane concentrations (K_{pl} , Z_{veg} , f_{root} , f_{grow} and $f_{pl,C_{Me}}$, respectively) (equation (8))⁴³. R_{pl} depends on ecosystem-specific plant functional types and increases in warmer soil due to the increase in vegetation growth. In both wetland and upland ecosystems, the 1-m soil profile was divided into 1 cm layers and the soil temperature, soil moisture and methane dynamics of TEM were simulated at daily time-steps⁹.

$$F_{div}(z,t) = -D(z,t)\frac{\partial C_{Me}(z,t)}{\partial t} \dots \quad (6)$$

$$R_c(z,t) = K_e f_{e(C_{Me}(z,t))} \dots \quad (7)$$

$$R_{pl}(z,t) = K_{pl}Z_{veg}f_{root}(z)f_{grow}(t)f_{pl,C_{Me}}(z,t) \dots \quad (8)$$

Permafrost TEM-HAM model. We first revised the TEM to consider PSOC dynamics and HAMs, but not $MIC_{biomass}$ changes (PTEM-HAM). We modified the Michaelis–Menten constant for methane oxidation from 5 to $0.11\ \mu M$ ($k_{Me,HAM}$) to consider atmospheric methane oxidation by HAMs^{2,23} (equation (9)). We set the maximum lower boundary of the soil layer from 1 m to 3 m to account for PSOC that is accessible as the surface temperature increases and the permafrost thaws. We then added PSOC dynamics by changing the main carbon source for MGs to vegetation (NPP) and PSOC (equation (10)). PSOC(z) represents PSOC stored at depth z ($g\ m^{-2}$) and is available when soil temperature at the corresponding depth is greater than $1^\circ C$. We set $PSOC_{max}$ as $300\ kg\ m^{-2}$ for top 3 m soil on the basis of NCSCDv2 (ref. ¹⁶). Accordingly, methane production and oxidation equations for PTEM-HAM are similar to equations (2) and (4), but $f(S_{OM})$ and $f(C_{Me})$ are replaced with $f_{new}(S_{OM})$ and $f_{new}(C_{Me})$, respectively (equations (11) and (12)).

$$f_{new}(C_{Me}(z,t)) = \frac{C_{Me}(z,t)}{k_{Me,HAM} + C_{Me}(z,t)} \dots \quad (9)$$

$$f_{new}(S_{OM}(z,t)) = \left(\left(1 + \frac{NPP_{mon}}{NPP_{max}}\right)f(C_{DIS}(z)) + \frac{PSOC(z)}{PSOC_{max}}\right) \dots \quad (10)$$

$$M_{prod,PTEM-HAM}(z,t) = M_{GO}f_{new}(S_{OM}(z,t))f(T_{soil}(z,t))f(H(z,t))f(X(z,t)) \dots \quad (11)$$

$$M_{oxid,PTEM-HAM}(z,t) = O_{max}f_{new}(C_{Me}(z,t))f(T_{soil}(z,t))f(E_{SM}(z,t))f(R_{ox}(z,t))f(N_{dp}(z,t))f(D_{MS}(z,t)) \dots \quad (12)$$

XPTM-XHAM. We further added explicit microbial dynamics of MGs and HAMs into PTEM-HAM (XPTM-XHAM). Methane oxidation by LAM was simulated as a function of environmental parameters with fixed $MIC_{biomass}$ (equations (4)) due to the limited control of LAM $MIC_{biomass}$ on Arctic wetland methane emissions^{29,30}. We ran additional simulations by adding microbial dynamics of LAM into XPTM-XHAM to clarify the role of LAM microbial dynamics in wetland methane emission for both contemporary period and future projection (Supplementary Methods 6 and Supplementary Fig. 16).

Methane production by MGs ($M_{prod,XPTM-XHAM}$) and oxidation by HAMs ($M_{oxid,XPTM-XHAM}$) are calculated by the product of $MIC_{biomass}$ and methane production and oxidation of PTEM-HAM ($M_{prod,PTEM-HAM}$ and $M_{oxid,PTEM-HAM}$), respectively (equations (13A) and (13B))⁴⁴. Active microbial biomass changes ($dMIC_{biomass}/dt$) are calculated thermodynamically by considering ϵ , m_E and the Gibbs free energy (ΔG) of MGs and HAMs (equations (13C) and (13D)). Here, the maximum methane production and oxidation potentials (M_{GO} and O_{max} , respectively, in equations (11) and (12)) are multiplied by a geometric parameter ($\gamma_{geometric}$) and become M'_{GO} and O'_{max} ($M'_{GO} = M_{GO} \times \gamma_{geometric}$ and $O'_{max} = O_{max} \times \gamma_{geometric}$), where the units for M'_{GO} and O'_{max} are $\mu M_{SOC} \mu M_{bioc}^{-0.66}\ h^{-1}$ and $\mu M_{CH_4} \mu M_{bioc}^{-0.66}\ h^{-1}$, respectively.

$$M_{prod,XPTM-XHAM} = MIC_{biomass,MG}^{2/3} \times \gamma_{geometric} \times M_{prod,PTEM-HAM} \dots \quad (13A)$$

$$M_{oxid,XPTM-XHAM} = MIC_{biomass,HAM}^{2/3} \times \gamma_{geometric} \times M_{oxid,PTEM-HAM} \dots \quad (13B)$$

$$\frac{dMIC_{biomass,MG}}{dt} = \epsilon_{MG} \times \left(0.8 \times MIC_{biomass,MG}^{1/3} \times \gamma_{geometric} \times M_{prod,PTEM-HAM} + MIC_{MG} \frac{m_E}{\Delta G_{r,MG}}\right) \dots \quad (13C)$$

$$\frac{dMIC_{biomass,HAM}}{dt} = \epsilon_{HAM} \times \left(0.8 \times MIC_{biomass,HAM}^{1/3} \times \gamma_{geometric} \times M_{oxid,PTEM-HAM} + MIC_{HAM} \frac{m_E}{\Delta G_{r,HAM}}\right) \dots \quad (13D)$$

Equations for changes in $MIC_{biomass}$ were derived from the growth rate (ΔP)⁴⁴, which is proportional to the relative magnitude in the difference between maintenance energy demand and rate of energy delivery of a metabolic redox equation in equations (13E) and (13F), where ΔP is in $kJ\ \mu mol_{biomass}^{-1}\ s^{-1}$, ΔG_r is the free energy of the metabolic redox reaction (which is usually negative) at in situ temperatures, activities and fugacities in $kJ\ \mu mol_{reactant}^{-1}$ and m_E is the maintenance energy in $kJ\ \mu mol_{biomass}^{-1}\ h^{-1}$. We assumed that only 80% of the free energy is available for metabolism and the rest is lost as heat⁴⁴.

$$\Delta P_{MG} = -0.8 \Delta G_{r,MG} M_{prod,PTEM-HAM} - m_E \dots \quad (13E)$$

$$\Delta P_{HAM} = -0.8 \Delta G_{r,HAM} M_{oxid,PTEM-HAM} - m_E \dots \quad (13F)$$

The rate of increase or decrease of active biomass is governed by the fraction of ΔG , that is directed to maintenance and the growth efficiency, so the active

biomass increases according to equations (13G) and (13H), where $MIC_{biomass}$ is in $\mu\text{mol}_{biomass} \text{ l}^{-1}$ and ε is in $\mu\text{mol}_{biomass} \mu\text{mol}_{substrate}^{-1}$.

$$\frac{dMIC_{biomass, MG}}{dt} = \frac{\varepsilon_{MG} \times MIC_{biomass, MG} \times \Delta P_{MG}}{-\Delta G_{r, MG}} \dots \quad (13G)$$

$$\frac{dMIC_{biomass, HAM}}{dt} = \frac{\varepsilon_{HAM} \times MIC_{biomass, HAM} \times \Delta P_{HAM}}{-\Delta G_{r, HAM}} \dots \quad (13H)$$

Here, ΔG_r is calculated using the net thermodynamic driving force (F_{thermo}) of the reaction in equation (14), where m is the number of moles of ATP generated per mole of reactant and ΔG_{phos} is the free energy for the phosphorylation reaction. At the point at which the thermodynamic drive vanishes, $\Delta G_r = -m \times \Delta G_{phos}$. For methanotrophs $\Delta G_{r, HAM} = -286 \times 2.8 \text{ kJ mol}^{-1}_{reactant} = -800.8 \text{ kJ mol}^{-1}_{reactant}$ (ref. 45). Whereas for MGs, the free energy of the metabolic redox reaction is much smaller, $\Delta G_{r, MG} = -25 \text{ kJ mol}^{-1}_{reactant}$ (ref. 46).

$$F_{thermo} = -\Delta G_r - m \times \Delta G_{phos} \dots \quad (14)$$

Finally, in equations (13A–D) we added the power of two-thirds to the active biomass term to account for substrate diffusion to the cell surface. Microbes rarely exist as single microbes in isolation, but rather as aggregates⁴⁷. As the availability of substrate is assumed to be positively correlated with diffusion, the rate of diffusion to the cell wall is thus determined by surface area (not cell volume). Based on this argument, as $MIC_{biomass}$ in equations (13C) and (13D)) does not cancel out, we calculated the theoretical $MIC_{biomass}$ at equilibrium, which is the maximum $MIC_{biomass}$ for given environmental conditions when MGs and HAMs are not limited by space (equations (15A) and (15B)).

$$MIC_{biomass, MG} = \left(\frac{-0.8 \times \gamma_{geometric} \times \Delta G_{r, MG} \times M_{prod, PTEM-HAM}}{m_E} \right)^3 \dots \quad (15A)$$

$$MIC_{biomass, HAM} = \left(\frac{-0.8 \times \gamma_{geometric} \times \Delta G_{r, HAM} \times M_{oxid, PTEM-HAM}}{m_E} \right)^3 \dots \quad (15B)$$

The $MIC_{biomass}$ changes in equations (13C) and (13D)) are dependent on ε and m_E . We set ε as 0.05 and 0.5 for MG and MT, respectively, defined from previous laboratory and experiment studies^{20,25,27,48}. The temperature sensitivity of m_E is derived from work by Tjihuis et al.²⁸, who studied a large range of different organisms and found that maintenance energy is mainly influenced by temperature (T , in °C) with an energy of activation of 69 kJ mol^{-1} (equation (16)).

$$m_E = 4.5 \times e^{\left(\frac{-6.94 \times 10^4}{k} \left(\frac{1}{T} - \frac{1}{298} \right) \right)} \dots \quad (16)$$

The initial $MIC_{biomass}$ of MG and HAM is estimated from metagenomic data (0.0002 and 0.0025 $\mu\text{mol}_{biomass} \text{ l}_{soil}^{-1}$, respectively)^{8,45,49}. We set the maximum $MIC_{biomass}$ of MG and HAM of each layer, as the maximum concentration of cells is 10^4 – 10^7 cells per gram of dry soil due to substrate availability and space limitation⁵⁰. Using conversion factors (1 cell = $8 \times 10^{-15} \text{ mol C}$, 1 soil = 1,500 g of dry soil) and the ratio of HAM and MG in the total microbial composition from Stackhouse et al.⁴⁵ (maximum 1.5% of total cells), we estimated that the maximum concentrations of both MG and HAM are 50,000 $\text{nmol}_{biomass} \text{ l}_{soil}^{-1}$.

Model optimization. We optimized a total of five parameters for upland methane oxidation and four parameters for wetland methane production related to both PTEM-HAM and XPTEM-XHAM (Supplementary Tables 1 and 2). All other parameters were set the same as in Zhuang et al.⁹ for methane production and transport processes and as in Zhuang et al.¹⁰ for methane oxidation. We first collected observation data from six sites representing uplands and wetlands for alpine tundra, wet tundra and boreal forest ecosystems to optimize these parameters^{4,6,51–53} (data from the Greenland Ecosystem Monitoring Programme were provided by the Department of Bioscience, Aarhus University, in collaboration with the Department of Geosciences and Natural Resource Management, Copenhagen University) (Supplementary Table 1). Aside from the observed meteorology from field sites, we also used CRU time-series data version 4.01 to fill missing meteorological inputs³¹. We then used the Shuffled Complex Evolution Approach in R language (SCE-UA-R) to minimize the difference between simulated and observed methane emission and consumption rates⁵⁴. For each site, 40 ensembles were run using SCE-UA-R with 10,000 maximum loops per parameter ensemble, and all of them reached steady state before the end of the loops. Our optimization results show that both XPTEM-XHAM and PTEM-HAM reasonably capture the magnitude and seasonality of observed soil methane fluxes (Supplementary Figs. 1 and 3).

Simulation for the contemporary period. *Set-up.* We used spatially explicit data of vegetation, soil pH and textures, meteorology and leaf area index to make spatially and temporally varying estimates of methane emission and consumption in the Arctic⁹. The vegetation and soil texture data sets were used to assign vegetation-

and texture-specific parameters to a grid cell^{42,55}. The soil-water pH dataset was used to estimate methane production across the study region⁵⁶. Meteorological inputs were derived from gridded CRU time-series data, v.4.01 (ref. 31). We used monthly leaf area index data derived from satellite imagery⁵⁷ to prescribe leaf area index for each 0.5° latitude and longitude grid cell. Finally, for PTEM-HAM and XPTEM-XHAM, we added the NCSCDv2 to estimate PSOC¹⁶. PSOC of each 1 cm of soil layer depth was calculated using the NCSCDv2 data by dividing the PSOC data of 1 m, 2 m and 3 m depths equally into different depths.

The model was applied at the spatial resolution of 0.5° latitude by 0.5° longitude north of 50°N for both wetland and upland ecosystems with an hourly time-step for microbial dynamics and a daily time-step for other processes and modules during 2000–2016. A year of spin up was used for methane equilibrium in soils for TEM and PTEM-HAM, and five years of spin up were used for biomass equilibrium in soils for XPTEM-XHAM. Simulated ecosystem-specific methane emission from wetlands and consumption from uplands were then area weighted for each grid cell, as defined by the static fractional inundation data³³.

Model-data comparison. *Site-level.* We compared our model results with data from 46 in situ measurements organized by Emmerton et al. and Lau et al. (Supplementary Table 5)⁵⁷. Specifically, Emmerton et al. summarized methane fluxes measured in high-, low- and sub-Arctic tundra for a portion of the northern growing season (May to October). Fluxes were organized by chamber and eddy covariance measurements and by terrestrial sites predominantly emitting or consuming methane. Lau et al. summarized methane emission and consumption in the northern circumpolar permafrost region, organized by soil pH, moisture, temperature, SOC and vegetation types for field measurements only. Due to a possible mismatch of soil and vegetation properties, and wetland distribution of grid cells between model and observation, we compared observed fluxes with simulated fluxes averaged over the growing season from 2000 to 2016 within two adjacent grid cells (1° × 1°) of the observation.

Regional level. We compared model simulations of three regions with methane emission (Alaska, Hudson Bay Lowlands, West Siberian Lowlands) and two regions with consumption (Northeast and West Greenland) (Supplementary Tables 6 and 7). Regional estimates of methane consumption were calculated by extrapolating the measured consumption from fields to a regional level after considering the heterogeneity of land ecosystems⁴⁶. Regional estimates of methane emission of previous studies were calculated by combining field measurements with an atmospheric inversion^{13–15}.

Pan-Arctic level. We compared the simulated net regional methane emission with results from a top-down inversion system, CarbonTracker-CH₄, CarbonTracker-CH₄ estimated anthropogenic and natural methane emission from 2000 through 2010 north of 50°N (ref. 11). To produce posterior flux estimates, CarbonTracker-CH₄ uses the ensemble Kalman smoother described by Peters et al.⁵⁸, and the TM5 transport model with driving meteorology from the European Centre for Medium-Range Weather Forecasting⁵⁹. Air samples from 88 surface flask-air methane measurements from the National Oceanic and Atmospheric Administration's cooperative global air sampling and tall tower networks were used to constrain the flux estimates. Measurements of methane from flask-air samples collected from light aircraft were used to evaluate the inversion results.

Simulation for future projection. *Set-up.* From 2017 to 2100, we used the IPCC future climate scenarios from RCP climate-forcing datasets, RCP 2.6, RCP 4.5 and RCP 8.5 (Supplementary Fig. 12). RCPs 2.6, 4.5 and 8.5 are climate projections with a possible range of radiative forcing values of 2.6, 4.5 and 8.5 W m^{-2} , respectively, in the year 2100³². As RCP datasets did not provide water vapour pressure data, we used the specific humidity and sea level air pressure from the RCP data sets and elevation of surface to estimate the monthly surface vapour pressure⁶⁰. Under those scenarios, the global climate was simulated with Hadley Centre Coupled Model v.3 at a 0.5° spatial resolution. Transient atmospheric methane data were obtained by linearly interpolating the decadal data for these future projections. Spatial data of vegetation, soil texture, soil pH and LAI used in the twenty-first century were the same as in the simulation for the contemporary period. Models were then applied at a spatial resolution of 0.5° latitude by 0.5° longitude north of 50°N for both wetland and upland ecosystems from 2017 to 2100. Our simulation showed the largest increase in soil temperature and moisture for RCP 8.5 followed by RCP 4.5 and 2.6, but the soil moisture increase was not distinct (Supplementary Fig. 12).

Microbial physiology. To elucidate effects of microbial physiological responses of MG and HAM to temperature increase, we conducted sensitivity tests by setting m_E as a function of temperature in equation (16).

Data availability

The data are archived and freely available at the Purdue University Research Repository (PURR) at: <https://purrr.purdue.edu/publications/3284/1> (<https://doi.org/10.4231/Q3R8-SZ17>).

Code availability

The code is also archived and freely available at the Purdue University Research Repository (PURR) at: <https://purrr.purdue.edu/publications/3284/1> (<https://doi.org/10.4231/Q3R8-SZ17>).

References

42. Zhuang, Q. et al. Modeling soil thermal and carbon dynamics of a fire chronosequence in interior Alaska. *J. Geophys. Res. D* **108**, 8147 (2003).
43. Walter, B. P. & Heimann, M. A process-based, climate-sensitive model to derive methane emissions from natural wetlands: application to five wetland sites, sensitivity to model parameters, and climate. *Global Biogeochem. Cy.* **14**, 745–765 (2000).
44. Lau, M. C. Y. et al. An oligotrophic deep-subsurface community dependent on syntrophy is dominated by sulfur-driven autotrophic denitrifiers. *Proc. Natl Acad. Sci. USA* **113**, E7927–E7936 (2016).
45. Stackhouse, B. T. et al. Effects of simulated spring thaw of permafrost from mineral cryosol on CO₂ emissions and atmospheric CH₄ uptake. *J. Geophys. Res. Biogeosciences* **120**, 1764–1784 (2015).
46. Thauer, R. K., Kaster, A. K., Seedorf, H., Buckel, W. & Hedderich, R. Methanogenic archaea: ecologically relevant differences in energy conservation. *Nat. Rev. Microbiol.* **6**, 579–591 (2008).
47. Gottschalk, G. *Bacterial Metabolism* (Springer Science & Business Media, 2012).
48. Von Stockar, U., Maskow, T., Liu, J., Marison, I. W. & Patiño, R. Thermodynamics of microbial growth and metabolism: an analysis of the current situation. *J. Biotechnol.* **121**, 517–533 (2006).
49. Stackhouse, B. et al. Atmospheric CH₄ oxidation by Arctic permafrost and mineral cryosols as a function of water saturation and temperature. *Geobiology* **15**, 94–111 (2017).
50. Conrad, R. The global methane cycle: recent advances in understanding the microbial processes involved. *Environ. Microbiol. Rep.* **1**, 285–292 (2009).
51. Sellers, P. J. et al. BOREAS in 1997: experiment overview, scientific results, and future directions. *J. Geophys. Res. Atmos.* **102**, 28731–28769 (1997).
52. Harazono, Y. et al. Temporal and spatial differences of methane flux at arctic tundra in Alaska. *Mem. Natl Inst. Polar Res.* **59**, 79–95 (2006).
53. Dinsmore, K. J. et al. Growing season CH₄ and N₂O fluxes from a subarctic landscape in northern Finland; from chamber to landscape scale. *Biogeosciences* **14**, 799–815 (2017).
54. Duan, Q. Y., Gupta, V. K. & Sorooshian, S. Shuffled complex evolution approach for effective and efficient global minimization. *J. Optim. Theory Appl.* **76**, 501–521 (1993).
55. Melillo, J. M. et al. Global climate change and terrestrial net primary production. *Nature* **363**, 234–240 (1993).
56. *Global Soil Data Task (IGBP-DIS, ISO-image of CD)*. (International Geosphere-Biosphere Program, PANGAEA, 2000); <https://doi.org/10.1594/PANGAEA.869912>
57. Myneni, R. B. et al. Global products of vegetation leaf area and fraction absorbed PAR from year one of MODIS data. *Remote Sens. Environ.* **83**, 214–231 (2002).
58. Peters, W. et al. An ensemble data assimilation system to estimate CO₂ surface fluxes from atmospheric trace gas observations. *J. Geophys. Res. Atmos.* **110**, D24304 (2005).
59. Krol, M. et al. The two-way nested global chemistry-transport zoom model TM5: algorithm and applications. *Atmos. Chem. Phys.* **5**, 417–432 (2005).
60. Seinfeld, J. H., Pandis, S. N. & Noone, K. Atmospheric chemistry and physics: from air pollution to climate change. *Phys. Today* **51**, 88 (1998).

Acknowledgements

This work was supported by NASA Earth and Space Science Fellowship Program (grant no. 80NSSC17K0368 P00001) and NASA Interdisciplinary Research in Earth Science (grant no. NNX17AK20G). B.E. acknowledges Danish National Research Foundation (grant no. CENPERM DNR100) for financial support. We also thank W. Wieder for providing model results and valuable discussions.

Author contributions

Y.O., Q.Z., M.C.L., T.C.O. and D.M. conceived the study. Y.O., Q.Z. and L.L. built the model. L.D., B.E. and G.H. provided unpublished or raw data. Y.O. conducted the model runs. All authors contributed to data interpretation and preparation of manuscript text.

Competing interests

The authors declare no competing interests.

Additional information

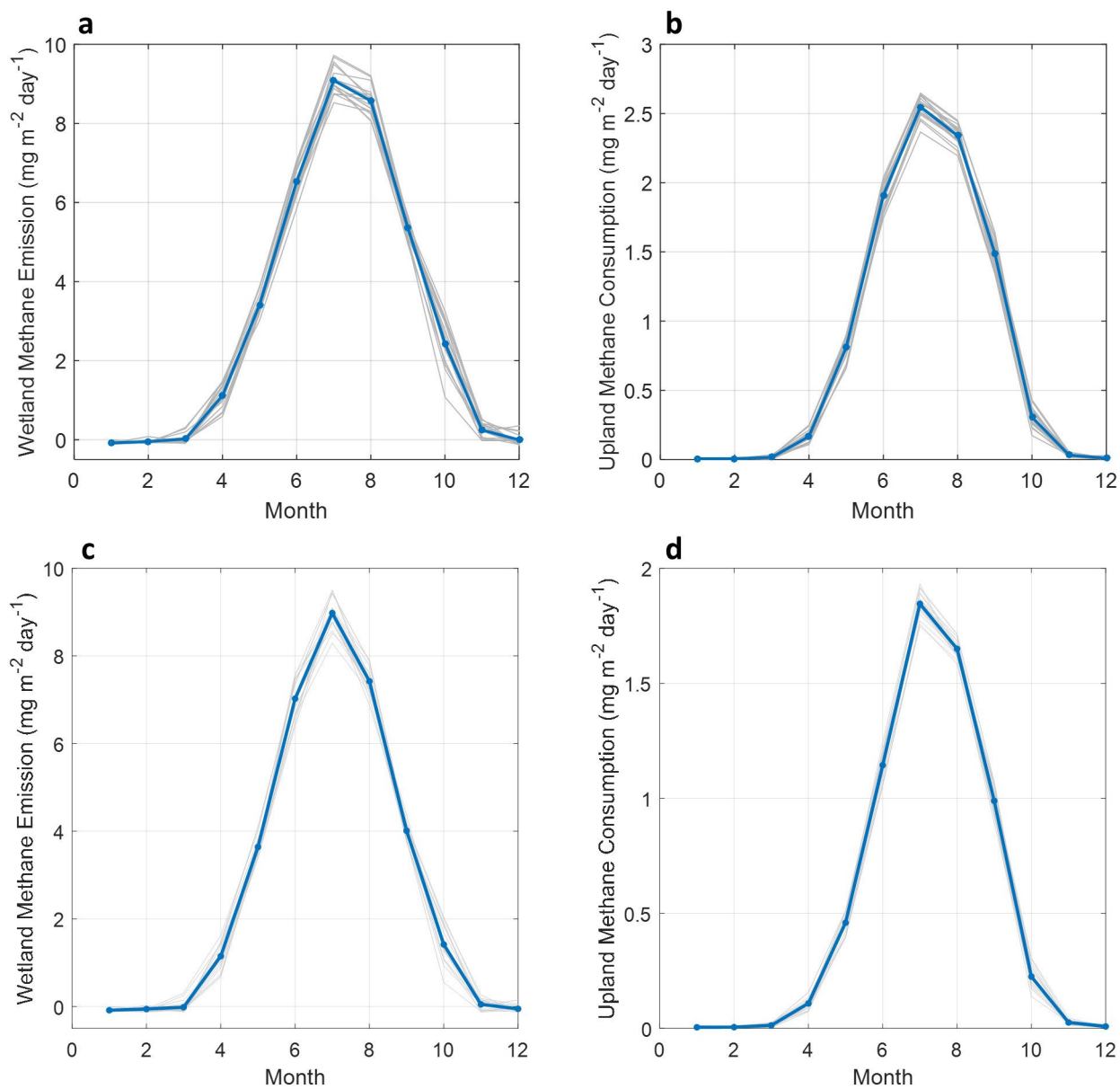
Extended data is available for this paper at <https://doi.org/10.1038/s41558-020-0734-z>.

Supplementary information is available for this paper at <https://doi.org/10.1038/s41558-020-0734-z>.

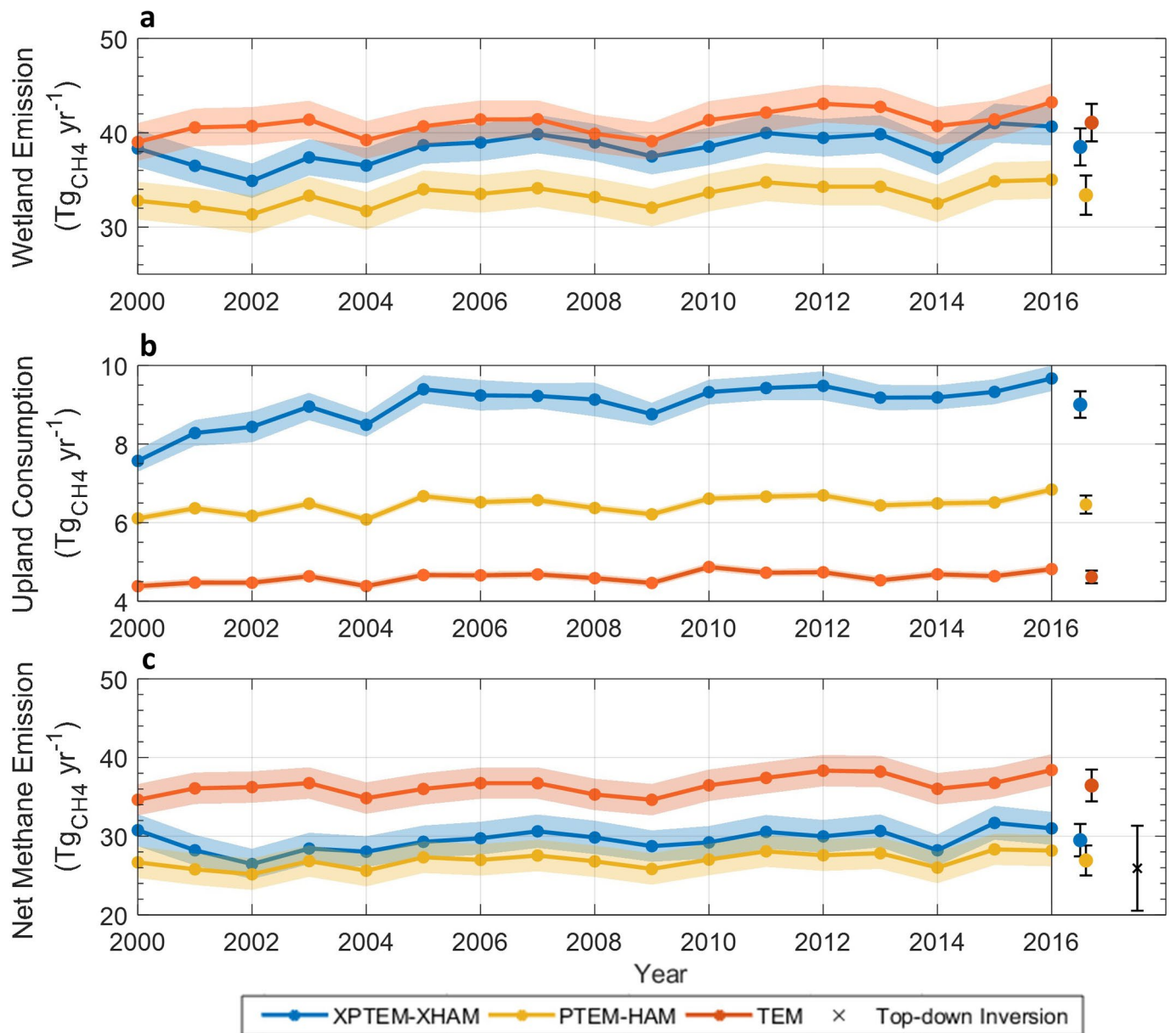
Correspondence and requests for materials should be addressed to Q.Z.

Peer review information *Nature Climate Change* thanks Lauren Hale and the other, anonymous, reviewer(s) for their contribution to the peer review of this work.

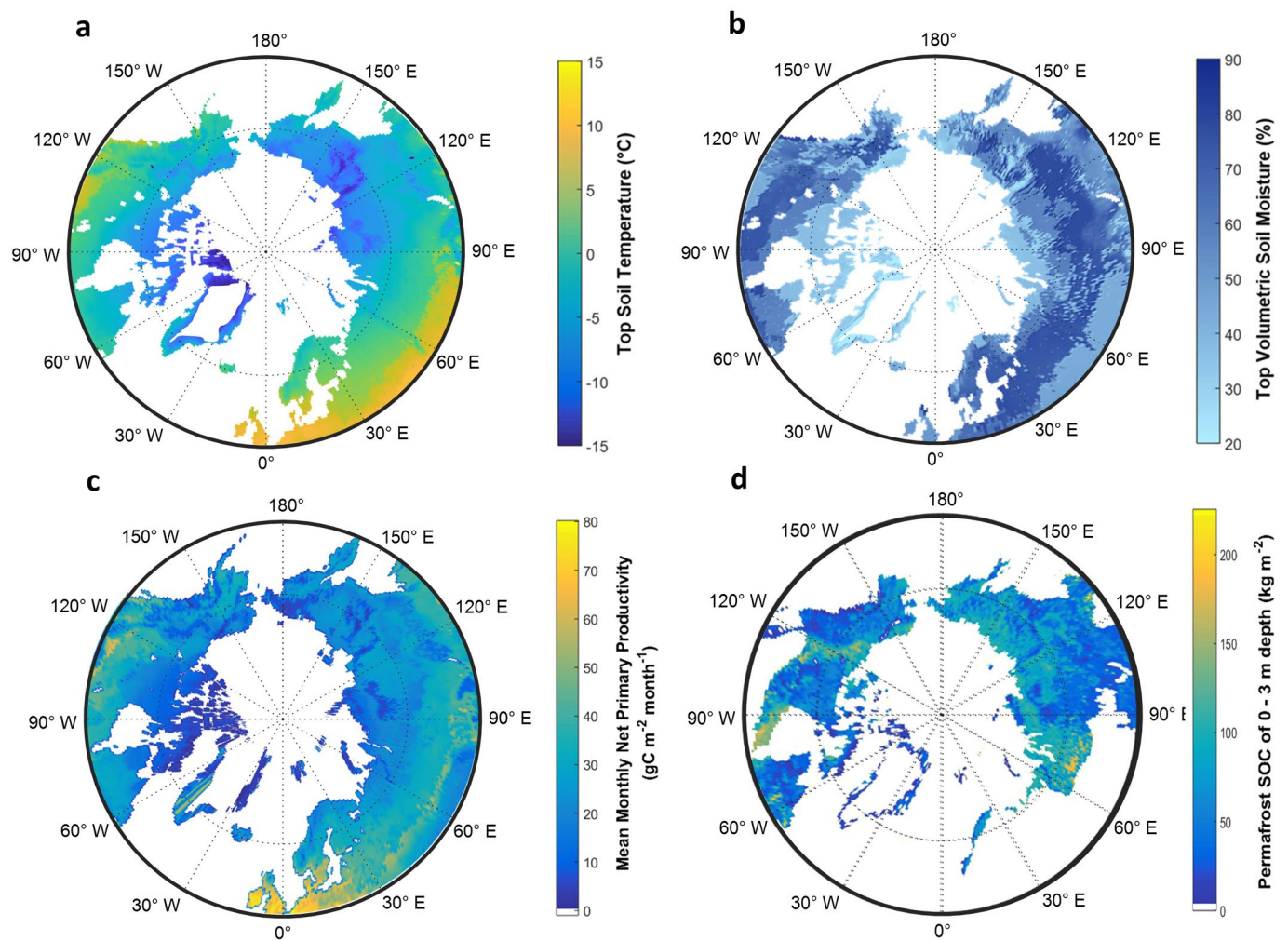
Reprints and permissions information is available at www.nature.com/reprints.



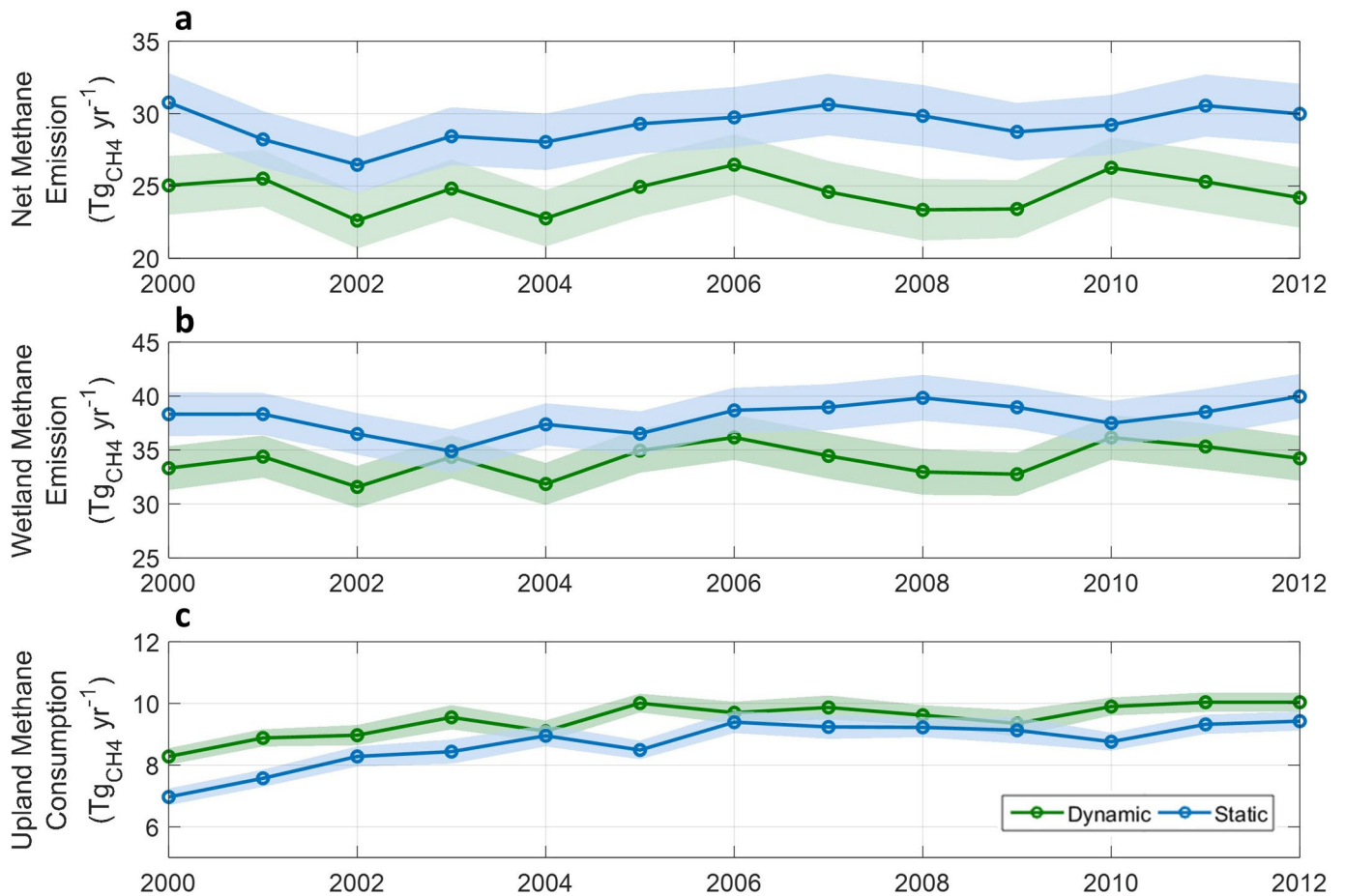
Extended Data Fig. 1 | Pan-Arctic monthly mean methane fluxes for XPTM-XHAM and PTEM-HAM from 2000-2016 north of 50°N. Estimates of pan-arctic (a, c) monthly wetland methane emission and (b, d) monthly upland methane consumption in mg m⁻² day⁻¹ for (a, b) XPTM-XHAM and (c, d) PTEM-HAM model. The blue line is monthly averages over 2000-2016, and grey lines represent values of each year.



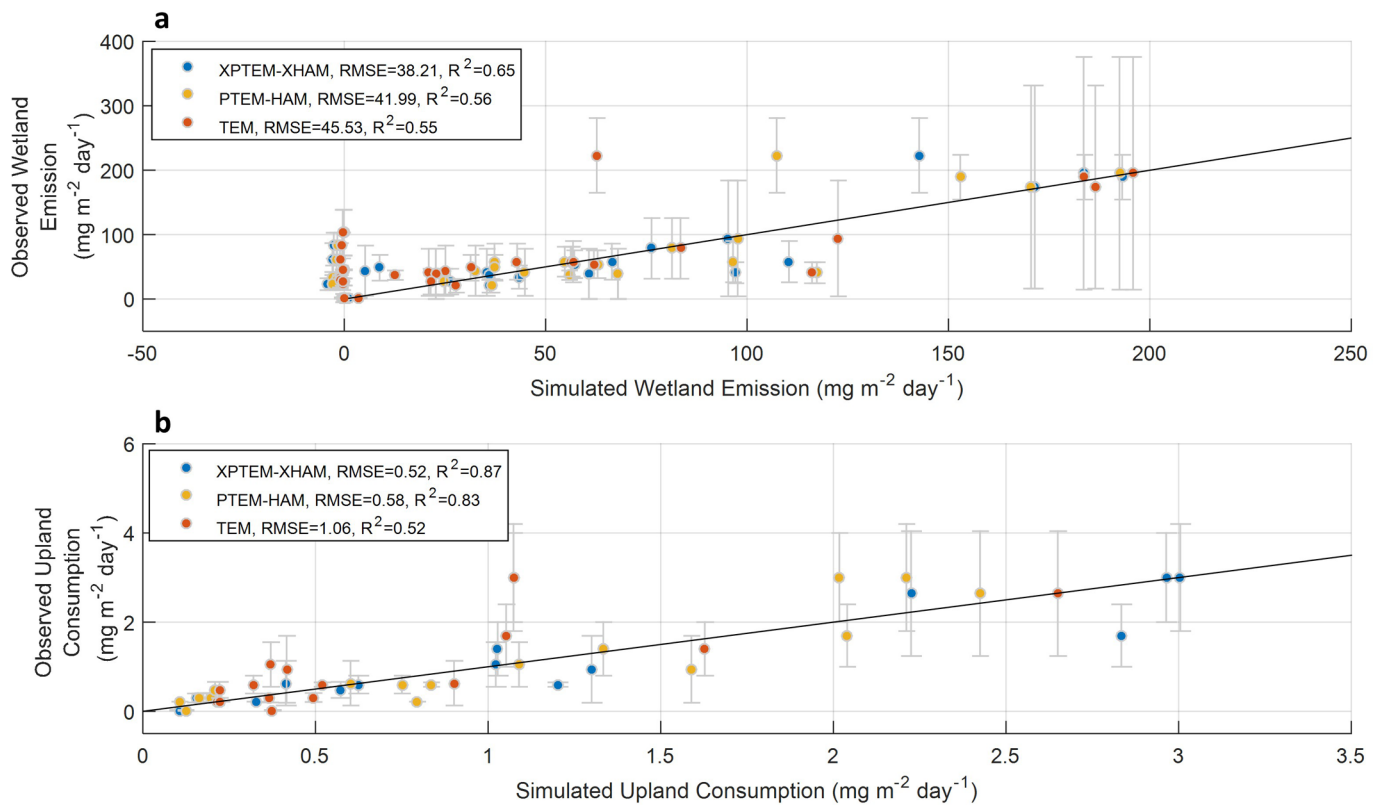
Extended Data Fig. 2 | Inter-annual variability of methane fluxes from 2000 - 2016 north of 50°N. (Left) Annual estimates of pan-arctic (a) wetland methane emission, (b) upland methane consumption, and (c) net methane emission for XPTEM-XHAM (blue), PTEM-HAM (yellow), and TEM (red) in $\text{Tg}_{\text{CH}_4}\text{yr}^{-1}$ from 2000-2016. The shaded area represents one standard deviation of models determined by varying the optimized parameters. (Right) Mean and one standard deviation averaged over the simulation period for each metric are given by the bars. Panel (c) additionally shows mean and one standard deviation of previous estimates of net methane emission estimated by top-down inversions (times symbol) by the bars.



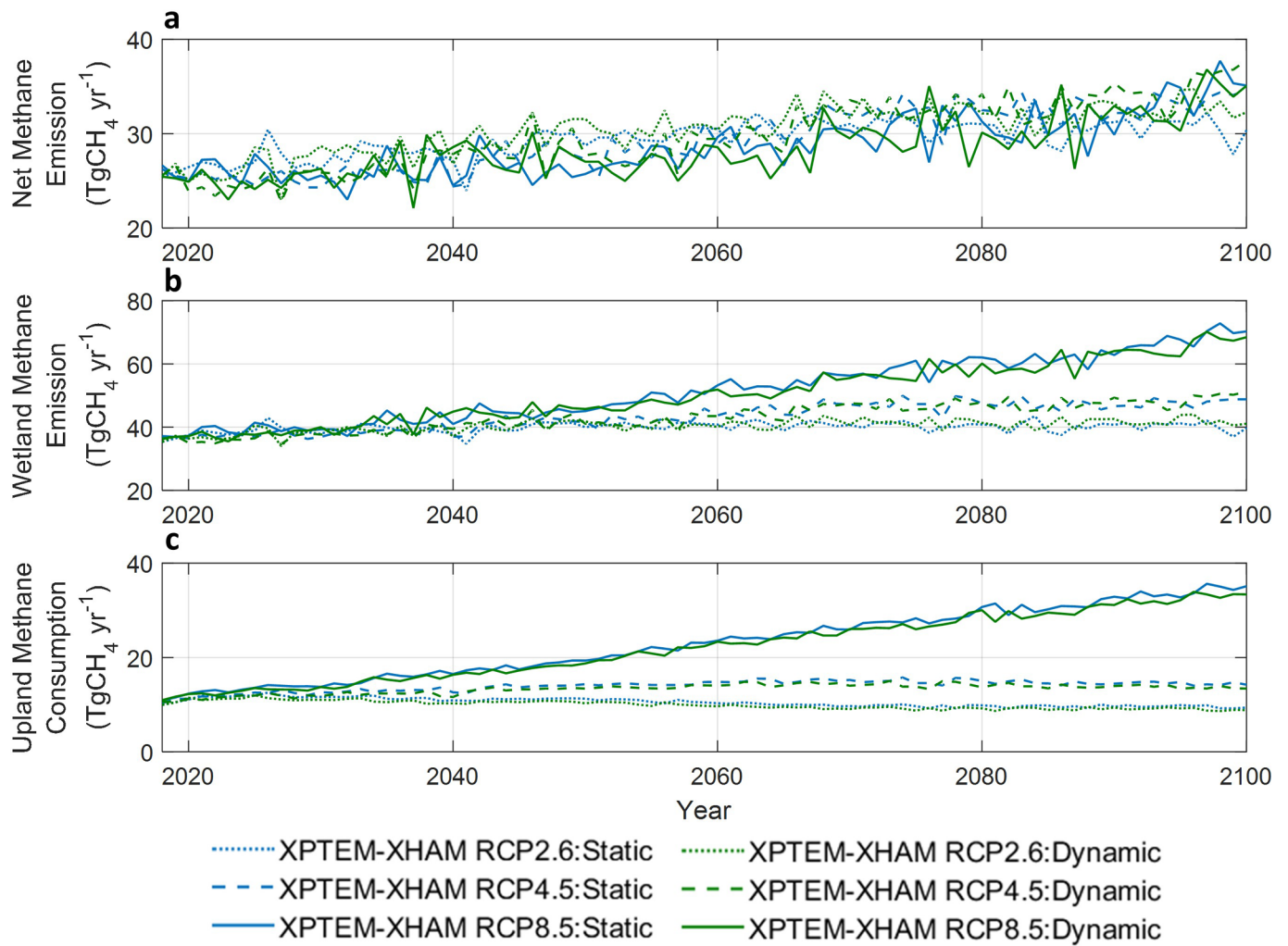
Extended Data Fig. 3 | Spatial variability of soil and vegetation properties north of 50°N. (a) annual top 10-cm soil temperature in °C, (b) annual top 10-cm soil moisture in % volume, (c) monthly net primary productivity in gC m⁻² month⁻¹, and (d) permafrost SOC stored in the top 3-m in kg m⁻²^{23,16}. The soil temperature, moisture, and net primary productivity were averaged over the contemporary period during 2000-2016. The dotted longitudinal lines are at 30° intervals, and the latitudinal line is at 65°N.



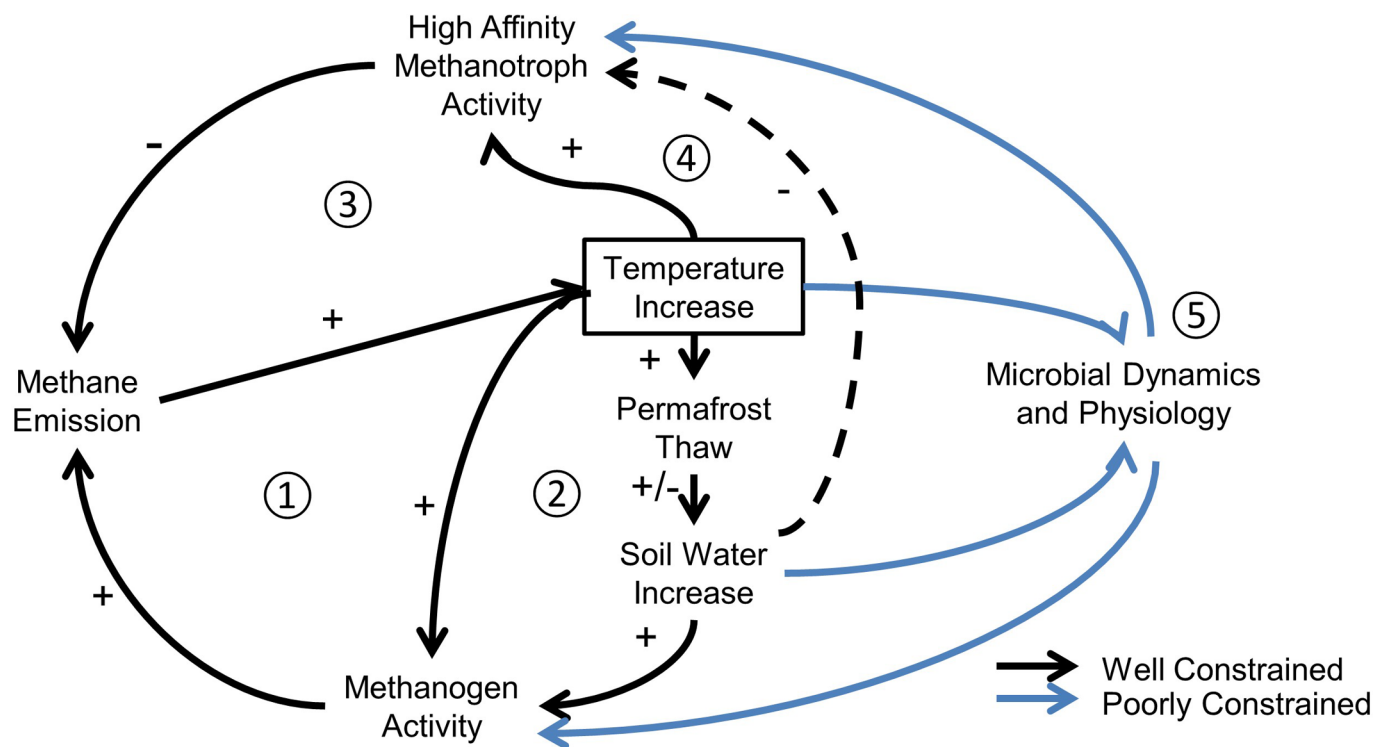
Extended Data Fig. 4 | Inter-annual variability of methane fluxes using time-varying inundation fraction from 2000 - 2012 north of 50°N. Annual estimates of pan-arctic (a) net methane emission, (b) wetland methane emission, and (c) upland methane consumption for XPTM-XHAM model using static inundation fraction³³ (blue) and time-varying inundation fraction from SWAMPS-GLWD³⁴ (green) in $\text{Tg}_{\text{CH}_4}\text{yr}^{-1}$. The shaded area represents one standard deviation determined by varying the optimized parameters.



Extended Data Fig. 5 | Model-data comparison of methane fluxes using site-level data. Comparison of (a) wetland methane emission and (b) upland methane consumption of data from 46 in situ measurements (supplementary table 5) with simulation results from XPTEM-XHAM (blue), PTEM-HAM (yellow), and TEM (red).



Extended Data Fig. 6 | Inter-annual variability of methane fluxes using time-varying inundation fraction from 2017 - 2100 north of 50°N. Annual estimates of pan-Arctic (a) net methane emission, (b) wetland methane emission, and (c) upland methane consumption for XPTM-XHAM model using static inundation fraction (blue) and dynamic inundation fraction (green) in $\text{TgCH}_4 \text{ yr}^{-1}$ using RCP 2.6 (dotted), RCP 4.5 (dashed), and RCP 8.5 (solid).



Extended Data Fig. 7 | Future Arctic methane feedbacks. Previous studies predicted a positive feedback between temperature increase and methane emission (circles 1-2). However, because high-affinity methanotrophs may respond strongly to temperature and less strongly to soil moisture due to uncertain Arctic hydrology (circles 3-4), this feedback may be partially suppressed. Moreover, explicit modeling of microbial dynamics (circle 5) will facilitate future model developments that include effects of microbial physiology (modified Fig. 5 of Oh et al.,⁸).